



HAL
open science

Development of Porous Ti64 by Partial Densification in Spark Plasma Sintering for Laminar Flow Control

Baptiste Egreteau, Fabien Méry, Cécile Davoine, Olivier Vermeersch, Marc Thomas

► **To cite this version:**

Baptiste Egreteau, Fabien Méry, Cécile Davoine, Olivier Vermeersch, Marc Thomas. Development of Porous Ti64 by Partial Densification in Spark Plasma Sintering for Laminar Flow Control. *Advanced Engineering Materials*, 2024, pp.2401096. 10.1002/adem.202401096 . hal-04753677

HAL Id: hal-04753677

<https://hal.science/hal-04753677v1>

Submitted on 25 Oct 2024

HAL is a multi-disciplinary open access archive for the deposit and dissemination of scientific research documents, whether they are published or not. The documents may come from teaching and research institutions in France or abroad, or from public or private research centers.

L'archive ouverte pluridisciplinaire **HAL**, est destinée au dépôt et à la diffusion de documents scientifiques de niveau recherche, publiés ou non, émanant des établissements d'enseignement et de recherche français ou étrangers, des laboratoires publics ou privés.



Distributed under a Creative Commons Attribution - NonCommercial - NoDerivatives 4.0 International License

Development of Porous Ti64 by Partial Densification in Spark Plasma Sintering for Laminar Flow Control

Baptiste Egreteau,* Fabien Méry, Cécile Davoine, Olivier Vermeersch, and Marc Thomas

The purpose of this study is to develop a porous material in Ti64 by partial densification with spark plasma sintering to be used as a porous panel for laminar flow control by suction. An important characteristic of porous panels for this application is their permeability, which must be as high as possible. The permeability can be related to the material's porous network. This is why samples are made by varying their manufacturing parameters (temperature, pressure, powder particle size, and powder quantity). Then, their permeability is measured experimentally, and their porous network is described with the measurement of porosity, local diameter distribution, and tortuosity thanks to X-ray tomography. The tortuosity measurements highlight the anisotropic effect of pressure on the porous network. The morphological parameters are used in a Kozeny–Carman model, which should predict porous materials' permeability, and be confronted with the experimental measurements. Finally, this characterization process leads to the selection of the best manufacturing parameters for the application.

1. Introduction

In the context of climate change, interest in fuel consumption reduction technologies for commercial airliners has been renewed. A way to achieve it is to lower drag, which has two main origins: pressure and skin friction. Skin friction is directly related to the boundary layer, the near-wall flow region with an important velocity decay in the wall-normal direction due to viscous

effect. The skin friction is proportional to the velocity gradient in the wall normal direction.^[1,2] This boundary layer can be either laminar, which means the flow is smooth and regular, or turbulent, where the flow is chaotic, with many vortices developing. The key point is that the skin friction coefficient is an order of magnitude higher for the turbulent boundary layer than the laminar one.


Given the turbulent airflow that airliners currently experience, extending the laminar flow region could lead to significant fuel savings. This is feasible for lifting surfaces, and extensive research on the subject has been conducted since the 1940s, as noted by Braslow.^[3] A way to do so is to apply wall suction through a porous surface. Currently, these suction devices are implemented in hybrid laminar flow

control (HLFC) systems as described by Krishnan et al.^[4]

This study focuses on the manufacturing and characterization of a porous material to make panels for laminar flow control by suction. The requirements for these panels are as follows: they must exhibit maximum permeability to reduce the power demands of the suction system, ensure uniform suction distribution to prevent three-dimensional disturbances, and minimally disrupt the grazing flow over their surface. Currently, laser microdrilled titanium sheets are the reference as presented by Young et al.^[5] A recent flight test on an A320 fin incorporating an HLFC concept used microdrilled titanium panels over 20 chambers around the leading edge.^[6] This article highlights several key challenges for the HLFC concept, with the primary one being the reduction of system complexity, weight, and manufacturing cost. This can be addressed by decreasing the number of chambers. Thus, the permeability of the panels should be evolutive. A first approach would be to vary the hole diameter or the pitch distance. Another recent solution proposed by Seitz et al.^[7] is called tailored skin single duct, where micro-perforated panels are associated with metallic meshes to control the pressure loss through the panel. The tailored combination enables variable permeability along the airfoil. A more original possibility is to use panels made of sintered metal powders. With the progress in powder metallurgy, new opportunities can be explored to make near-net shape panels with scalable porosity and more complex pore networks that will modify the materials' permeability. Indeed, some tests of laminar flow control with sintered porous panels have already been made.

B. Egreteau, F. Méry, O. Vermeersch
DMPE
ONERA
Université de Toulouse
31000 Toulouse, France
E-mail: baptiste.egreteau@onera.fr

C. Davoine, M. Thomas
DMAS
ONERA
Université Paris-Saclay
92320 Châtillon, France

 The ORCID identification number(s) for the author(s) of this article can be found under <https://doi.org/10.1002/adem.202401096>.

© 2024 The Author(s). Advanced Engineering Materials published by Wiley-VCH GmbH. This is an open access article under the terms of the Creative Commons Attribution-NonCommercial-NoDerivs License, which permits use and distribution in any medium, provided the original work is properly cited, the use is non-commercial and no modifications or adaptations are made.

DOI: 10.1002/adem.202401096

Braslow et al. led a pioneering study on laminar flow control with a porous sintered bronze skin.^[8] It proved incomplete sintered metal could be effective but encountered issues due to surface defects. More recently, Egreteau et al.^[9] also performed a flow control experiment with a porous sintered stainless steel sheet. This panel was at least as efficient as reference laser microdrilled titanium sheets. Nevertheless, this was done with off-the-shelf porous materials not designed for this application. This is why it would be interesting to develop porous material by partial sintering specially dedicated to flow control by suction as it has been done with many processes for biocompatible implants, for example, see refs. [10–12]. Here, it was chosen to work with spark plasma sintering (SPS) and Ti64 powder. Indeed, Ti64 is a reference titanium alloy that is already well known. As for SPS, it is an original process in the sintering family for which porous materials with titanium alloys have already been made.^[13–15] Moreover, few studies have been conducted on the influence of SPS process parameters on the properties of the resulting materials. Xie et al.^[16] studied the effect of pressure application by SPS on the thermal conductivity anisotropy of melt-spun $(\text{Bi, Sb})_2\text{Te}_3$. They showed that a high SPS pressure induced a preferred orientation of grains, resulting in a higher anisotropy factor for the thermal conductivity. Cao et al.^[17] studied the influence of powder oxidation on the anisotropy of the mechanical response of Al made by SPS. They found that powder oxidation increased anisotropy in tensile mechanical properties. To our knowledge, no studies have been conducted on the possibility of increasing permeability by obtaining an anisotropic porous network in the flow direction. This anisotropy would be an advantage since a material with a preferred transport direction in the flow direction could have the same permeability as an isotropic material while being less porous and then having a better mechanical strength.

This article presents the manufacturing protocol of porous Ti64 by partial densification in SPS. The influence of manufacturing parameters (pressure and temperature in the first

order and the particle size and quantity in the second order) on the samples permeability and pores morphology will be studied. Samples permeability will be experimentally determined and their porous network morphology will be described using X-ray tomography scans (porosity, local diameter, and tortuosity). The morphological data will be input in a Kozeny–Carman (KC) model to predict the samples permeability. This model has been already employed to predict metal foams permeability.^[18–20] This predicted permeability will be confronted with the experimental measurements. In the end, based on this characterization, the best manufacturing parameters for the flow control application will be selected.

2. Manufacturing Process

This section will introduce the manufacturing technique used here (SPS) and detail the samples manufacturing protocol.

SPS is a field-assisted sintering process where powder is sintered quickly by the combined application of a strong electric current and uniaxial pressure, as illustrated on **Figure 1a**. It was first intended to sinter powder quickly with a high compaction rate near-net-shape parts with a fine microstructure.^[21] Nevertheless, as explained by Dudina et al.^[22] many ways exist to divert its use and make porous samples. Here, the partial densification method has been preferred for the sake of simplicity for the upscaling part. This means sintering is conducted in conditions (time, pressure, temperature) that do not allow to totally densify the powder. It means, the process is stopped after necks formation and before advanced densification to use the open porous network while having a solid enough part.

Temperature and pressure conditions were chosen to stay under the α/β allotropic temperature of Ti and inspired by the work discussed in refs. [13,14,23] which already sintered Ti-based alloys.

Two batches were made. The first one was made on the ONERA facility, which is a Thermal Technology DCS 200-40.

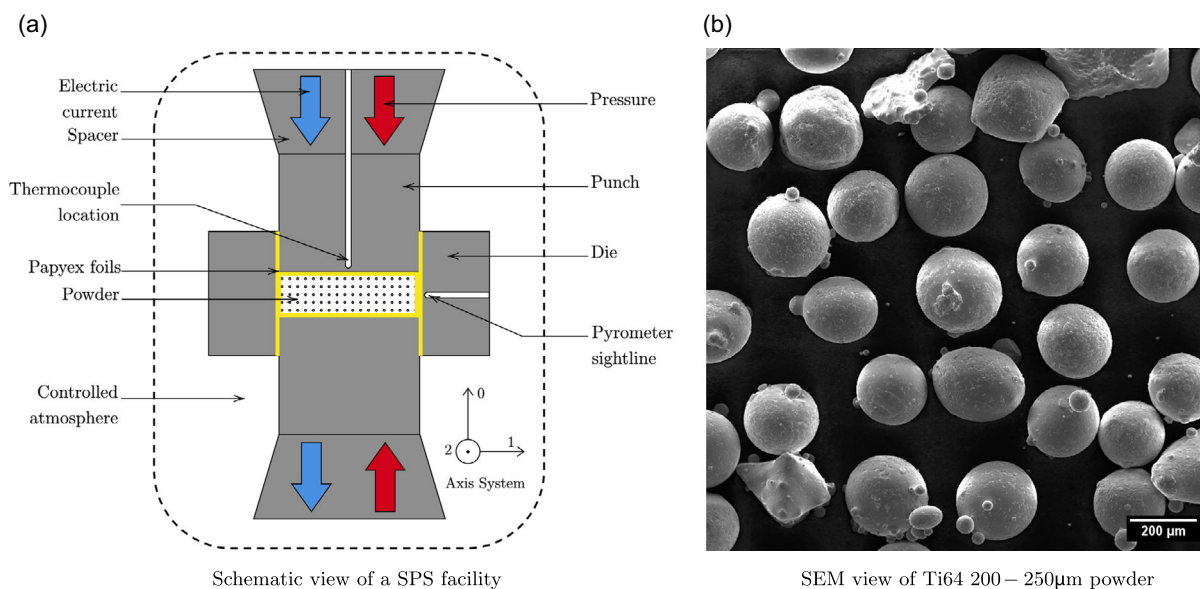


Figure 1. Presentation of a SPS facility and the Ti64 powder. a) schematic view of a SPS facility, b) SEM view of Ti64 200–250 μm powder.

Table 1. First batch manufacturing parameters on ONERA facility.

Sample	T750P05	T750P20	T800P05	T800P20	T850P05	T850P20
Temperature [°C]	750	750	800	800	850	850
Pressure [MPa]	5	20	5	20	5	20
Particle size [µm]	200–250	200–250	200–250	200–250	200–250	200–250
Powder mass [g]	15	15	15	15	15	15

This first batch aimed to study the influence of temperature and pressure on the pores everything else being equal. The 6 samples manufacturing conditions are gathered in **Table 1**. Here, the temperature was measured with a thermocouple placed in the center of the upper piston, 2 mm from the powder.

All other parameters were identical: the die inner diameter was 36 mm, the heating rate was set to 100 °C min⁻¹, dwell time was 5 min long, followed by free cooling, and a spherical Ti64 powder was used. As can be seen in Figure 1b, powder particles were mainly spherical with few satellites.

The second batch was made on the Sumitomo Dr Sinter 2080 facility from the National Flash Sintering Platform (PNF2) in Toulouse. The aim was to study the reproducibility of the first batch on another facility, the influence of powder quantity and particle size. Here, the temperature was measured with a pyrometer aimed at the side of the die. The 4 samples manufacturing conditions are gathered in **Table 2**.

All other parameters were identical: the die inner diameter was 36 mm, spherical Ti64 powder was used, the heating rate was set to 100 °C min⁻¹, dwell time was 5 min long, a 20 MPa pressure was applied, and followed by free cooling.

A coarse powder has been chosen to have large spaces between powder particles, thus ensuring a percolating porous network after sintering. The quantity of powder was chosen to make 3.2 to 4.5 mm thick pastilles to find a compromise between good sintering conditions and moderate pressure drop for permeability evaluation. Only the last sample (T800P20M8) was made thinner (1.9 mm), to study the effect of powder quantity and be closer to the panels thickness.

After manufacturing, the carbon paper, used to seal the die stuck to the samples, clogged the pores on the surface. To unclog the pores, the samples were polished on both sides. First, a coarse paper (P80) was used to effectively remove the carbon paper, followed by progressively finer grains (up to P4000) to remove the material that had “smeared over” the surface and blocked the pores. However, this polishing process would be difficult to set up for large-scale samples. During the manufacturing of these larger samples, carbon spray will be used instead to prevent this problem.

Table 2. Second batch manufacturing parameters on PNF2 facility.

Sample	T750P20	T800P20	T800P20G160	T800P20M8
Temperature [°C]	750	800	800	800
Pressure [MPa]	20	20	20	20
Particle size [µm]	200–250	200–250	125–160	200–250
Powder mass [g]	15	15	15	8

3. Characterization of the Samples Produced by Partial Sintering

Now, the samples need to be characterized to understand and anticipate their performances for HLFC application. To do so, optical microscope observations, permeability measurements, and analysis of their 3D porous network morphologies have been conducted.

3.1. Optical Microscope Observations

The first observations of the samples' porous network were made with an optical microscope (Zeiss Axio Vert.A1 MAT, magnification 5). In **Figure 2**, top views (i.e., along axis 0, the pressure application direction) of all batch 1 samples can be seen. These pictures show different degrees of densification without any particular organization between powder particles. It appears that on short temperature and pressure ranges, a wide variety of porosities is reachable. In the bottom left picture, which corresponds to the least advanced degree of sintering, necks are formed, but the process was stopped before volume densification started, leaving the powder particles clearly visible. Some small spherical pores can also be seen at the center of some particles. These pores seem closed and are certainly due to the powder-making process. The powder was made using an electrode induction gas atomization process, which leads to some gas entrapment during solidification. These small closed pores are useless for suction application but are not attributable to the SPS process. Then, the higher the temperature or pressure, the more volume densification occurred. The pores become smaller, and the boundaries between powder particles become more and more unclear.

Figure 3 shows the same samples observed from the side (i.e., normal to axis 0, the pressure application direction). If the samples porous network is anisotropic, there should be a difference in the pores arrangement between **Figure 2** and **3**. There might be more vertically oriented structures for T800P20 and T850P20 on **Figure 3**. X-ray tomography will enable to confirm this assumption by quantitatively measuring the morphology of the porous network in three dimensions.

3.2. Permeability Evaluation

Permeability can be defined as the capacity of a porous material to allow fluids to pass through it. For a given flow rate, the higher the permeability, the lower the pressure drop through the material. It is measured thanks to an experimental setup presented on **Figure 4**. An airflow is injected into a plenum and passes through the sample along axis 0, as defined in **Figure 1a**, via a known injection diameter. This allows us to measure the pressure drop from each side of the sample ($P_{\text{atmo}} - P_1$) and then apply the Darcy law (Equation (1)) to extract the material's permeability

$$-\frac{\Delta P}{L} = \frac{\mu}{K_D} V \quad (1)$$

where ΔP is the pressure drop on each side of the porous medium, L is the porous medium thickness, μ is the fluid

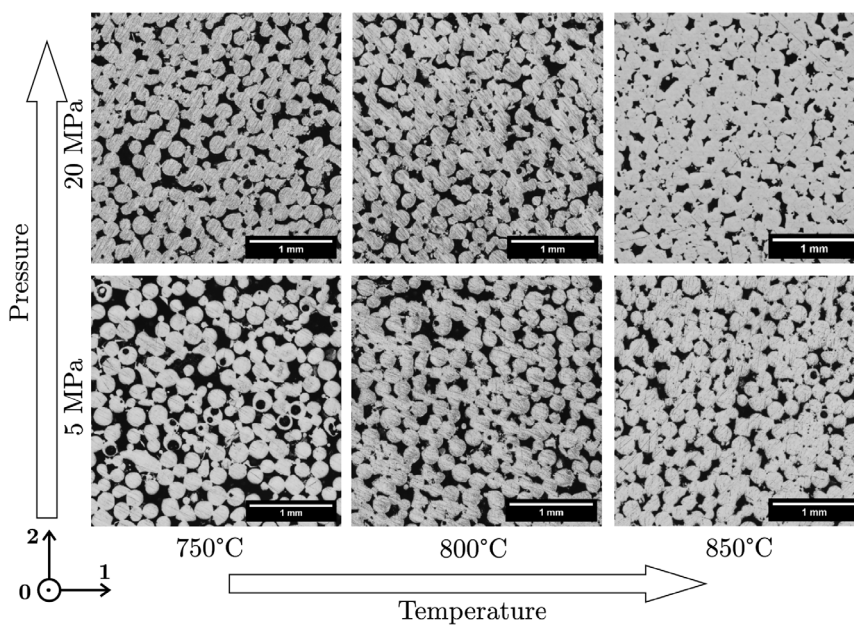


Figure 2. Optical microscope top views of batch 1 samples.

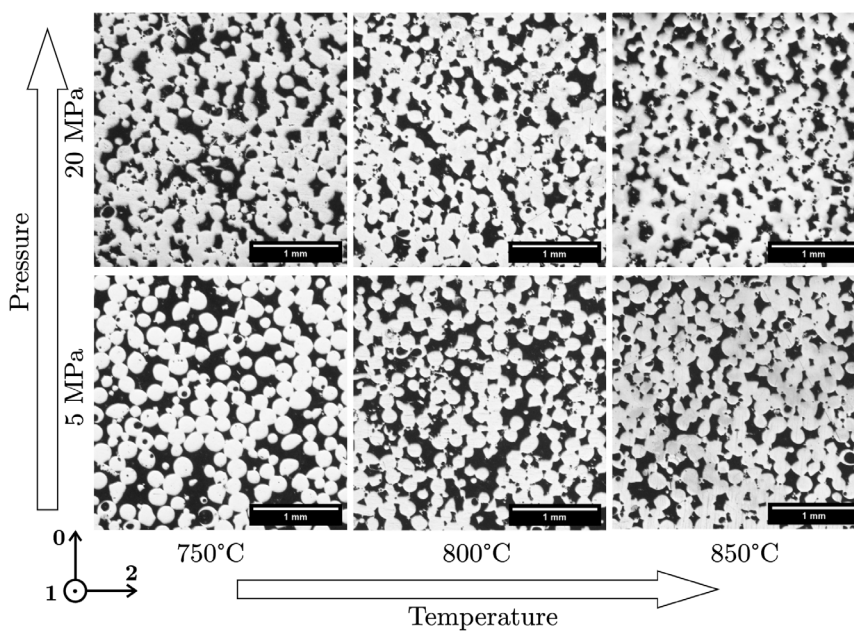


Figure 3. Optical microscope cross-section views of batch 1 samples.

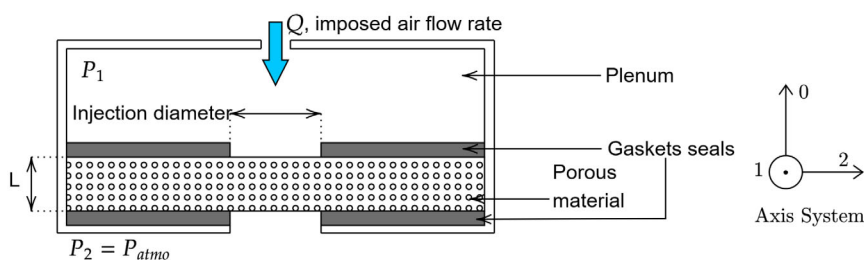


Figure 4. Sketch of the permeability test bench.

dynamic viscosity, V is the darcian velocity calculated by dividing the volumetric flow rate by the cross-sectional area, and K_D is the darcian permeability. As the fluid is air in our experiments, μ has been taken at $1.8 \times 10^{-5} \text{ kg ms}^{-1}$. The injection diameter was 20 mm.

K_D , which is associated to viscous effects, is an intrinsic value of a porous medium, as specified by Carman.^[24] It does not depend on the flow conditions (as long as it remains in a Darcy regime), nor on the sample's thickness. This is why it is a relevant characteristic to compare different material's permeability.

It has been determined that the Darcy law, and not the Darcy–Forchheimer one, was the most appropriate because the target suction velocity is up to 10 mm s^{-1} . At this suction velocity, it has been experimentally established that the relation between the pressure gradient and the suction velocity was linear and not quadratic.

For each sample, the measurements were realized three times and their mean values are gathered in **Table 3** and plotted on **Figure 10**.

The first information is that all samples are permeable. Then, as expected, it can be seen with batch 1 that the higher the temperature or the pressure, the lower the permeability as densification is pushed further. Comparing T800P20 and T750P20 between the two batches, we can also see that the permeability

is always higher for second-batch samples. Moreover, the permeability of laser-drilled titanium sheets used by Methel^[25] was measured on the same bench. K_D values were between 1×10^{-12} and $4.5 \times 10^{-12} \text{ m}^2$. This means that for the same panel thickness, there are manufacturing parameters such that the same pressure would be required to apply a given suction velocity for reference microdrilled titanium sheets and porous Ti64 made by SPS.

3.3. X-ray Computed Tomography (CT)

As explained previously, a 3D imaging technique is necessary to access the porous network structure. The choice fell on the X-ray tomography scans (CT scans). This imaging technology uses X-ray absorption by matter to reconstruct 3D images of its inner structure. It offers a good compromise between the resolution and the scanned volume, which needs to be large enough to describe the medium satisfactorily. The 3D image is composed of voxels (cubes) that are the 3D equivalent of 2D image pixels (squares). Each voxel has a greyscale value associated with material X-ray absorption at its location. An example of the 3D reconstructed scan can be seen in **Figure 5a**.

For each sample, a single specimen was extracted at its center to be scanned. It would have been interesting to extract specimens on the samples periphery to study sintering

Table 3. All samples characteristics.

Batch	Mass [g]	Particles size [μm]	Pressure [MPa]	Temperature [$^{\circ}\text{C}$]	Name	Thickness [mm]	K_D [m^2]	ϕ [%]	$\overline{d_{loc}}$ [μm]	$\sigma(d_{loc})$ [μm]	τ_0	τ_1	τ_2	I_{ani} [%]	K_{KC} [m^2]
1	15	200–250	5	750	T750P05	4.2	1.1×10^{-11}	32.0	69.1	28.4	1.9	2.1	2.0	5.3	1.0×10^{-11}
				800	T800P05	4.35	3.2×10^{-12}	26.7	53.9	24.4	2.6	2.7	2.4	-5.1	2.8×10^{-12}
				850	T850P05	3.35	1.7×10^{-13}	18.4	47.5	20.7	4.4	4.7	3.7	-5.6	5.4×10^{-13}
				750	T750P20	3.8	1.7×10^{-12}	22.4	51.5	22.1	3.0	3.4	3.6	15.3	1.7×10^{-12}
				800	T800P20	3.45	5.4×10^{-13}	17.7	46.6	20.0	4.6	6.0	5.9	22.7	4.5×10^{-13}
				850	T850P20	3.44	7.2×10^{-14}	13.1	40.9	17.9	6.6	9.7	10.5	28.8	1.1×10^{-13}
2	8	125–160 200–250	20	750	T750P20	3.35	4.0×10^{-12}	23.9	58.9	24.5	2.3	2.8	2.9	18.4	3.8×10^{-12}
					T800P20	3.8	1.1×10^{-12}	17.7	48.9	20.9	3.0	4.3	4.2	29.0	1.2×10^{-12}
				800	T800P20G160	3.15	5.0×10^{-13}	17.3	35.9	13.8	4.4	6.9	7.6	39.8	2.9×10^{-13}
					T800P20M8	1.87	2.1×10^{-13}	14.3	48.2	20.0	3.8	6.8	6.6	43.9	5.8×10^{-13}

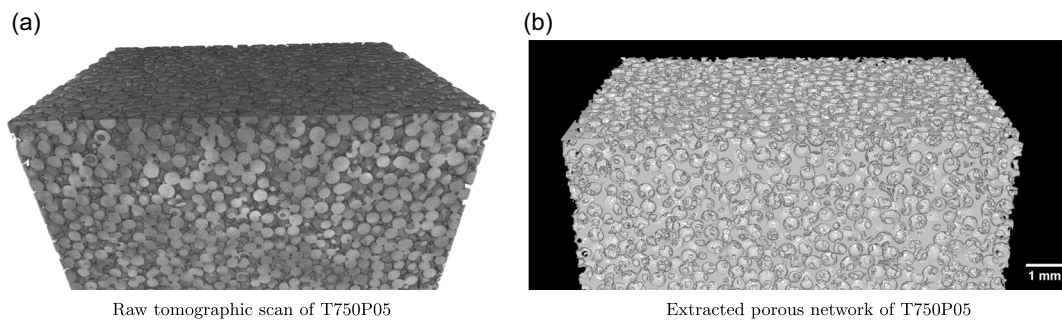


Figure 5. Tomographic scan and extracted porous network of SPS samples. a) raw tomographic scan of T750P05, b) extracted porous network of T750P05.

inhomogeneity, but it could not be done in the present study. A compromise had to be found between the scanned volume, that needs to be representative of the sample, and the resolution, which needs to be fine enough to capture small pores well. Our samples scanned volume was about $6 \times 4 \times 4 \text{ mm}^3$, with a resolution between 3.6 and $5 \mu\text{m}$, depending on the samples. The aim was to capture the entire thickness of the sample in a scan, as it is in this direction that air will be sucked, and to maximize the resolution.

Afterward, the CT scans were binarized to be usable by the characterization algorithms. This means distinguishing the voxels representing matter from those representing pore-space. It was done with an adequate threshold on greyscale value by using ImageJ software. An example of the binarized image is shown in Figure 5b, where the porous network is displayed. With this extracted porous network, evaluations on the samples porosity, pore network local diameter distribution, and tortuosity can be done.

3.3.1. Porosity

First, porosity can be computed. Porosity is the ratio between the volume of the pore space and the total volume of the sample. Two kinds of porosities can be distinguished: the open one and the closed one. An open pore lets air through the material, whereas a closed one does not. For HLFC application, the least amount of closed porosity is required, as it weakens the material without participating in air passage. Then, the open pores (those enabling to travel from the top to the bottom of the sample) were distinguished from the closed ones with the *trim_nonpercolating_paths* function from Porespy library.^[26] After this step, the interesting result was that there was always a single open pore in every CT scan. This is why it is preferred to talk about “open porous networks” rather than “open pores.”

As displayed in Figure 6 and summed up in Table 3, the samples open porosity (called ϕ) ranges from 13 to 32%. Whereas closed porosity is always below 0.3%. So, a huge majority of the pores are helpful for the HLFC application, but this high total porosity, compared with microdrilled sheets one ($< 1\%$), might be detrimental to mechanical performances. First, as expected, the higher the temperature and pressure, the lower the porosity. Batch 1 samples show a significant effect of temperature and pressure on the densification rate, as a wide range of porosity

can be reached through narrow temperature and pressure window (100°C , 15 MPa). Finally, reducing particle size does not seem to influence porosity because T800P20 and T800P20G160 have similar porosity. However, this is not the case for powder quantity, as T800P20M8 has a 3.4% lower porosity than T800P20. This information will be considered in the future because the final porous panels should be 2 mm thick or less (like T800P20M8), whereas our samples made with 15 g of powder are 3.5 to 4.5 mm thick.

In the next paragraphs, characterization will be made only on the open porous networks, as closed pores do not determine the material’s permeability measured previously.

3.3.2. Pore Network Local Diameter Distribution

It would now be interesting to determine the width of the channels constituting the open porous network. As we have a complex porous network, it is not possible to approximate pores with spheres or spheroids and extract their diameters. It is preferable to compute the local width of the porous network at any position within it. This statistical data will be called the pore network local diameter, noted d_{loc} . For a given porosity, if the channels forming the porous network are narrow, d_{loc} will be distributed over low values and the material permeability will be low. Whereas, for larger channels, d_{loc} will be distributed over high values and the material permeability will be higher. As the porous networks of our samples have no clear structuring element (such as a cylinder for a microperforated titanium sheet for example), a method not relying on geometrical assumptions has to be employed. This is the case of the ‘local thickness’ algorithm from the Porespy Python package,^[26] which computes for every voxel the diameter of the largest overlapping sphere that fits in the network. Then, the cumulative density function (cdf) of d_{loc} is plotted for each sample to visualize the distribution better. This cdf gives the fraction of pore space whose local pore diameter is lower than a given length. An example is visible on Figure 7 for the T850P20 sample. It shows half of the network’s local diameter is inferior to $47 \mu\text{m}$ and 95% of it is inferior to $80 \mu\text{m}$. The cdf is then compared with two statistical laws, normal and log-normal. It seems that a normal distribution is a relevant assumption, as it fits well with the measured cdf. The normal law cdf particularly fits well at high local diameters, which are the best defined in scan resolution. This good accordance with a

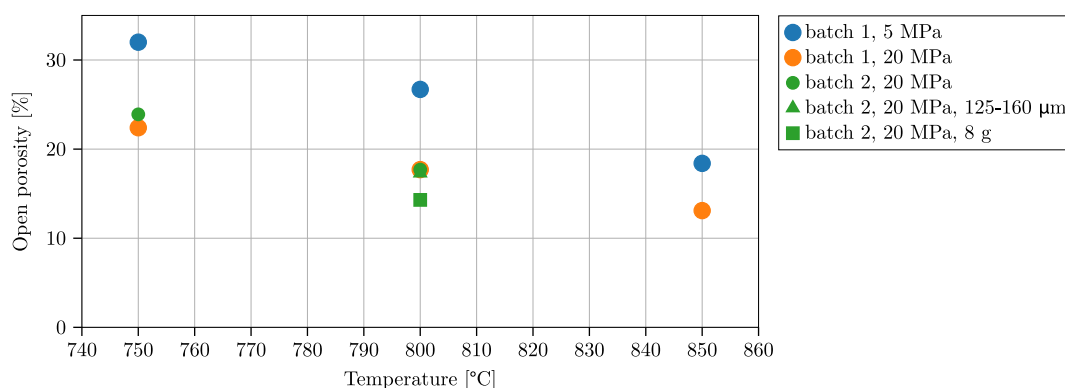


Figure 6. Samples open porosity.

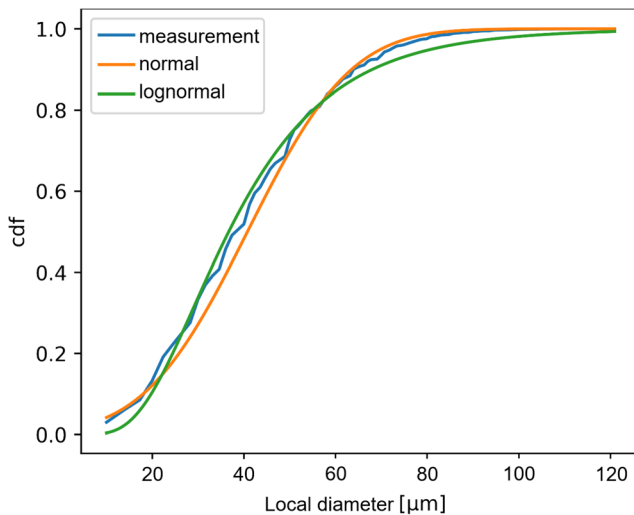


Figure 7. The cdf of T850P20 pore diameter (blue) and fits with normal (orange) and lognormal (red) statistic laws.

normal law has prompted us to describe the local diameter distribution with a mean local diameter, $\overline{d_{loc}}$, and a local diameter standard deviation, $\sigma(d_{loc})$. Then, it can be assumed that 95% of the network's local diameter is in the interval $[\overline{d_{loc}} - 2\sigma(d_{loc}), \overline{d_{loc}} + 2\sigma(d_{loc})]$. These data are plotted on **Figure 8** and gathered in Table 3.

Here are some comments about these data. First, the influence of pressure and temperature on the porous network's local diameter is clearly established with batch 1 samples. The further the sintering, the thinner the network. With a temperature range of 100 °C and a pressure range of 15 MPa, $\overline{d_{loc}}$ can be reduced by 41% and its 95% range by 37%. For reproducibility samples (T800P20 and T750P20 in both batches), second batch samples seem to have slightly larger network, which would be a first point to explain their greater permeability measured in paragraph 3.2. Then, powder quantity does not seem to influence the porous network's local diameter, as the distributions of T800P20 and T800P20M8 are very similar. Finally, as expected, the sample with finer powder (T800P20G160) has a clearly thinner network than T800P20. This is due to smaller gaps left between smaller particles, consistently with T800P20G160 lower permeability than T800P20.

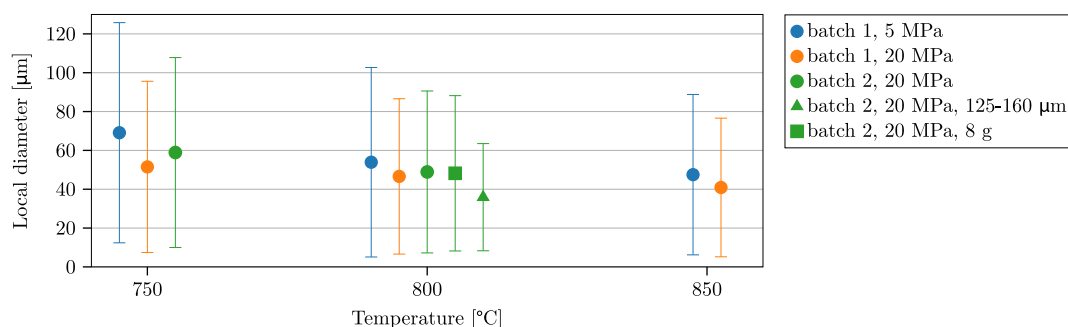


Figure 8. Samples local diameter distribution: mean local diameter, $\overline{d_{loc}}$, and 95% range, $2\sigma(d_{loc})$.

3.3.3. Tortuosity and Anisotropy

The last information extracted from the scan is the axial tortuosities. Tortuosity (usually noted τ) describes media transport properties, their sinuosity, and the complexity of internal percolation paths. However, it is not consistently formalized by every scientific field.^[27] In the present work, it was evaluated thanks to the Pytrax Python package,^[28] which relies on random walk inside the pore network. Indeed, particles are spread inside pore space and jump independently and randomly from one position to a neighboring one. For each time step, the axial square displacements (the mean square displacement component for a given direction) of the swarm are computed and compared with the one in free space. Tortuosity should then be seen as a ratio between diffusion coefficients in free space and in a porous medium for a given transport direction. Computations were made with 10^4 walkers during 10^7 time steps. This allowed us to evaluate tortuosity in the direction of pressure application, called here axis 0, and two orthogonal directions, called axes 1 and 2. The results for all the samples are gathered in Table 3. Thanks to batch one, it is seen the further the sintering, the higher the tortuosity in every direction. This is coherent with the evolution of pore size and porosity because these physical quantities are related to each other. Indeed, the thinner the pore space is, the more tortuous the path to go through.

To evaluate the porous network anisotropy, an anisotropy index is defined as follows

$$I_{ani} = \frac{\frac{2}{1/\tau_1 + 1/\tau_2} - \tau_0}{\frac{2}{1/\tau_1 + 1/\tau_2}} \quad (2)$$

where τ_0 is the tortuosity along the axis 0, the pressure application direction, τ_1 and τ_2 are the tortuosities along axes 1 and 2 perpendicular to the pressure application direction. It represents the relative difference between the tortuosity along axis 0 and the one in the plane defined by axes 1 and 2. As explained by Promentilla et al.^[29] the harmonic mean of axial tortuosities computes the tortuosity of a higher dimension space. This index is plotted for every sample in **Figure 9**. It shows a near-zero anisotropy for the samples sintered at 5 MPa, suggesting an isotropic pore space. Whereas, I_{ani} is significantly positive (from 15% to 44%) for samples sintered at 20 MPa in both batches, suggesting an anisotropic pore space with a preferred transport direction along axis 0.

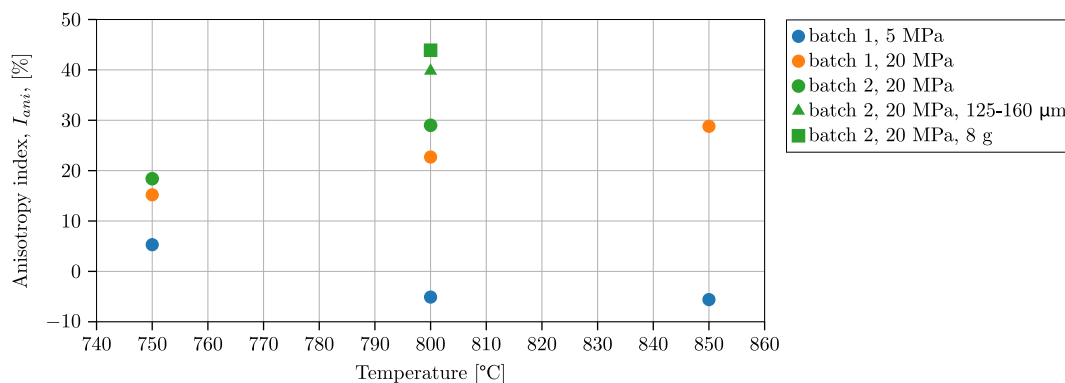


Figure 9. Samples anisotropy index.

4. Discussion

4.1. Influence of the Manufacturing Parameters on the Porous Network

The data extracted from the characterization protocol tend to demonstrate that temperature is the key parameter to control the densification rate of the powder. Indeed, over a very short range (100 °C), wide ranges of permeabilities and porosities are reachable. As shown in Figure 2, it is the parameter driving the volume densification and, thus, the final porosity. From that statement, it becomes important to measure it precisely and consistently to have repeatability in the process. This might explain the differences in permeability and porous network characteristics between T750P20 and T800P20 between batches 1 and 2. Indeed, as told in Section 2, the temperature was not measured the same way for both facilities. The pyrometer might have slightly overestimated temperature compared with the thermocouple, leading to a slightly lower sintering degree for these samples.

Furthermore, an anisotropy was noted for samples sintered at higher pressure (20 MPa) as can be seen on Figure 9. In these cases, tortuosity was always lower along axis 0 than in the orthogonal directions (axes 1 and 2). When computing the anisotropy index, it appears that τ_0 is always between 15% and 44% less than the orthogonal tortuosities harmonic mean. This effect might be

explained as follows. First, higher pressure might favor powder bed rearrangements, resulting in a more compact distribution. Then, the vertical pressure could favor contact between particles at their top and bottom. These preferred contact locations would be the site of formation of a greater number of sintering necks, resulting in a preferred sintering direction. This preferred sintering direction would lead to the formation of aggregates oriented along the pressure application direction (axis 0). These vertically oriented aggregates would then guide the pores in this same direction. Another possible effect may be attributed to the temperature. The relatively high temperature boosts the metal ductility. This higher ductility, combined with uniaxial pressure, could lead to the deformation of the particles, which would flatten out at their top and base, thus increasing their exchange surface locally. This would also result in a preferred sintering direction. These hypotheses should be confronted with a detailed study of sintering neck formation and growth between powder particles.

The sample made with a finer powder (T800P20G160) suggests that the particle size does not modify the sintering mechanisms since its porosity is similar to that of the T800P20 sample. The result is simply a thinner network, which explains its lower permeability. However, as shown in Figure 10 and 6, the permeability and porosity of T800P20M8 (1.9 mm thick) were lower than T800P20 (3.8 mm thick) in batch 2. This suggests that the sintering mechanisms might not be the same for thinner parts.

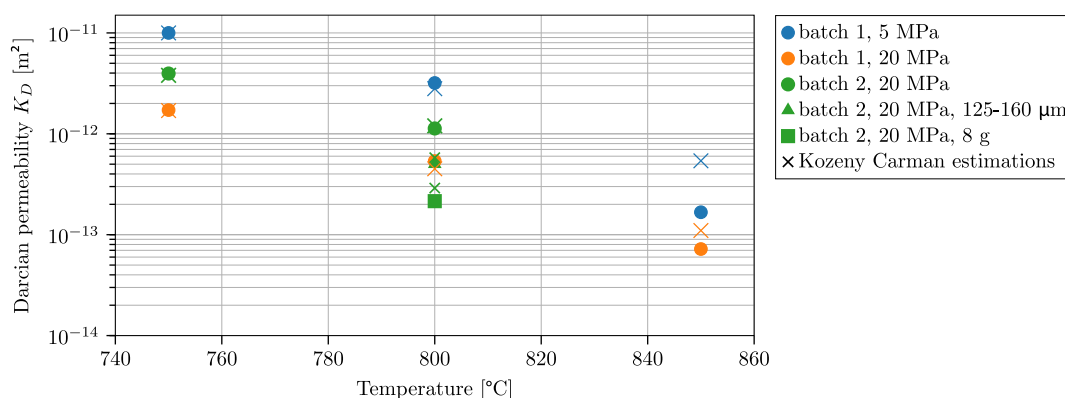


Figure 10. Comparison between measured permeabilities (full symbols) and those computed with KC model (crosses).

4.2. Reproducibility between Both SPS Facilities

Four samples were made with the same manufacturing parameters in batches 1 and 2 to study the reproducibility of the first batch in another facility. They were made at respectively 750 and 850 °C, 20 MPa, with 15 g of 200–250 μm powder. The differences between them in terms of permeability and pore network morphology are slight. All the data that will be mentioned here are gathered in Table 3. Batch 2 samples are about twice more permeable than batch 1 ones, which is a small difference for experimental permeability measurements. The porosity is slightly higher for batch 2 sample at 750 °C and identical at 800 °C. $\overline{d_{loc}}$ and τ_0 are respectively slightly higher and lower for batch 2 samples. This tells that batch 2 samples, which are moderately more permeable, also have a larger and less tortuous porous network. We make the assumption that this could be due to the way temperature is measured between both batches. Indeed, an overestimation of temperature for batch 2 samples would lead to a slightly lower temperature in the samples during manufacturing and, thus, a lower densification. In batch 1, the temperature was measured with a thermocouple placed at the center of the upper punch, near the powder. In batch 2, the pyrometer aimed in a sightline drilled in the die's side. Considering the short sintering time, it is likely that the thermal field was not completely homogeneous. Moreover, the porous Ti64 powder should have a lower electrical conductivity than the dense graphite that the die is made of. Then, most of the electric current might go through the die, heating the powder from the side. This could explain a slight temperature overestimation for batch 2. Nevertheless, the samples' characteristics are pretty close, which gives us confidence in the accuracy of the temperature measurements on both facilities.

4.3. Comparison with the KC Model

It has been seen that permeability and porous network morphology are correlated. As told by Kaviani,^[30] a model between permeability and microscopic morphology is a very complex problem due to the variety of porous network shapes, and only empirical or first-principle-based correlations with their own restrictions are available. Nevertheless, the materials studied here can be considered close to powder-packed beds. The flow regime through the material follows Darcy's law. This is why it was chosen to confront the experimental permeability results to a KC model. Dullien^[31] models permeability as follows

$$K_{KC} = \frac{\phi d_h^2}{16 k_0 \tau^2} \quad (3)$$

where ϕ is the open porosity, d_h is the hydraulic diameter defined as the ratio: $\frac{4 \times \text{Void volume}}{\text{Surface area}}$, k_0 is a shape parameter usually set between 2.0 and 2.5,^[24] and τ is the tortuosity.

The data computed from the CT scans are derived to feed the KC model. The porous network mean local diameter, $\overline{d_{loc}}$ determined in Section 3.3.2 was used as d_h , the axial tortuosity along axis 0, τ_0 , determined in Section 3.3.3 as τ and k_0 was set to 2.5. From there, permeabilities are calculated and compared to the

experimental permeability measurements as it can be seen on Figure 10 and in Table 3.

The agreement between measurements, K_D , and the KC model results, K_{KC} , is really good for the most porous samples. This is coherent, knowing that this kind of model was first developed to study the permeability of packed powder beds and natural stones, which the least sintered samples are similar to. Indeed, volume densification scarcely happened, and the porous network remains close to one of free powder before sintering. Nevertheless, the model's predictions differ greatly from the measurements (relative gap superior to 20%) for the samples sintered at 850 °C, the one made with less powder and the one made with finer powder. These samples have the lowest permeabilities, porosities, and porous network local diameter associated with the highest tortuosities. It could be because the mean local diameter is not representative of the hydraulic diameter anymore, or the KC model reach its limits for such low permeabilities (and thus such a dense material).

4.4. Selection of the Best Manufacturing Parameters

All the characteristics measured and exposed previously have been associated to select the most preferable material.

Permeability is an important feature that allows an essential degree of freedom to tune the material, especially in the perspective of an HLFC application on a complex wing shape where the material needs to have a permeability adapted to the pressure gradient along the airfoil. Young et al.^[5] and Schrauf et al.^[6] gave typical value of microdrilled sheets geometry for HLFC wing concepts. Holes are 50 μm diameter and 0.5 mm spaced, resulting in a porosity around 0.8%. Methel et al.^[32] also used two microdrilled panels for laminar flow control by suction over a flat plate model. Here, holes diameters were respectively 90 and 190 μm, spaced respectively by 1.6 and 1.44 mm. This is why, in the present study, the permeability of laser microdrilled sheets with similar holes diameter and spacing was measured on the same permeability test bench as the SPS samples. Their holes diameter ranged from 50 to 130 μm and their spacing from 0.5 to 1 mm. The K_D values of these panels ranged from 1×10^{-12} to $4.5 \times 10^{-12} \text{ m}^2$. Nevertheless, these panels do not represent the whole variety of microdrilled panels that might be used in an HLFC context. This is why, to enable some latitude in the selection, the material's permeability should be higher than $5 \times 10^{-13} \text{ m}^2$. This removes samples sintered at 850 °C. Indeed, their permeability is very low and thus not suitable for our application. The samples sintered at 800 °C propose a wide permeability range that is particularly well-suited for our application.

Then, tortuosity measurements highlighted the anisotropy of the porous network for samples sintered at 20 MPa. This anisotropy resulted in a preferred transport direction through the sample, which is exactly what is desired to apply suction through a panel. This is why, samples sintered at 5 MPa are rejected. A risk when applying suction for laminar flow control is to have local vertical overspeed creating a kind of aerodynamic roughness due to the streamtube. Schrauf et al.^[6] recalled some typical values of equivalent roughness to avoid due to the streamtube. This phenomenon is called oversuction and can destabilize the

laminar boundary layer, thus promoting the turbulence regime. It is favored when, at iso-airflow, porosity or pore size is reduced. T800P20G160 has a significantly thinner porous network: over 20% reduction of mean local diameter regarding the other samples. Finally, T750P20 and T800P20 are good candidates, but the least porous sample is preferred because it should also positively affect our material's mechanical behavior. Indeed, Oh et al. performed mechanical characterization of partially sintered samples fabricated from pure Ti powder by hot press^[12] and SPS.^[33] They determined the relation between the samples' Young's modulus and their porosity was affine for porosity values between 5% and 40%. Our sample's porosity are comparable with these values. Moreover, bulk Ti and Ti64 Young's modulus are similar (about 110 GPa). So, our samples Young's modulus can be estimated from these affine regressions. T800P20 Young's modulus would be around 60 GPa and T750P20 one around 48 GPa. Oh et al.^[12] also performed three-point bending tests on the same samples. This would be a relevant characterization for our samples because this would be the typical stress seen by the materials as skin panels on an aircraft wing. In the end, T800P20 seems to be the best choice to make a porous panel for laminar flow control by suction application.

Extensive recipe tests should be performed around this candidate's features to slightly modify the sintering temperature, pressure, or powder size to assess the range of material types one can reach. To avoid further extensive X-ray analysis, an acoustic inverse method could be interesting to be applied. Roncen et al.^[34] have shown that it is possible to solve the inverse problem of a porous material over an airgap, enabling microscopic parameters to be quantified using impedance measurements, and an appropriate model. This is exactly the configuration studied here. Indeed, if we use the Horoshenkov model,^[35] an acoustic impedance model for simple porous materials that take as an input three parameters (pore size, standard deviation on pore size, and porosity) applied to Roncen's inverse method, we can trace the microscopic dimensions of the material.

One next challenge is to make larger panels suitable for HLFC application; much work has to be carried out on upscaling studies. Indeed, these panels need to be thinner than the samples made here (3.2 to 4.5 mm thick). As mentioned in Section 4.1, thin parts might be more densified than thicker ones. Then, the sintering temperature might need to be lowered to reproduce T800P20 permeability for a thinner sample without losing its pores anisotropy. Moreover, larger dies should be required to make larger panels, and certainly not cylindrical ones. This will require a careful study of temperature distribution inside the sample during manufacturing because it has been demonstrated here that small temperature variations could greatly affect the material's performance. Ultimately, these panels will have to be tested aerodynamically in a wind tunnel. Initially, on simple academic configurations (such as a flat plate) before gaining in complexity (wing profile, then complete wing). For higher complexity configurations, the suction velocity needs to evolve chordwise. Currently, this is made with a succession of suction chambers, but it adds weight to the system. This is why making panels with an evolutive permeability would be interesting to reduce the number of suction chambers. It might be done by creating a temperature gradient during manufacturing by making a die with variable thickness. The panel's thickness might

also be evolutive by using a die and punches with variable heights. Finally, different powder particle sizes could also be used in the same panel with proper preparation before sintering.

5. Conclusion

In this article, the manufacturing and characterization of a porous Ti64 obtained by SPS with a partial densification method is presented. This material should be used in the future as a porous panel for laminar flow control by suction. The aim was to study the influence of temperature and pressure applied during sintering in the first order and the influence of particle size and quantity in the second order on the performances of the materials. We set up a characterization protocol to evaluate the materials' permeability and the morphology of their porous network (porosity, local diameter distribution, and tortuosity). This enabled us to reach the following conclusions: 1) Powder was successfully consolidated for each sample that was all permeable with a single open porous network; 2) Temperature and pressure are relevant control parameters as they allow to reach a wide range of permeabilities. These permeability values cover those of microdrilled sheets, which are the reference for porous panels dedicated to HLFC; 3) The tortuosity characterization highlighted the samples' anisotropic porous networks sintered at 20 MPa, whereas it is not the case for lower pressure; and 4) The permeability of the most porous samples was well predicted by the KC model with the data extracted from CT scans.

The performances reached with the T800P20 sample match the requirement for HLFC application, but extensive work still needs to be done to produce large-scale panels with this sample's characteristics.

Acknowledgements

This work has been partially funded by the NACOR project, within the frame of the Joint Technology Initiative JTI Clean Sky 2, AIRFRAME Integrated Technology Demonstrator platform being part of the Horizon 2020 Research and Innovation framework program of the European Commission (grant agreement no. 945521). The authors would like to thank Jean-Philippe Monchoux from CEMES, Université Paul Sabatier, Toulouse, for his support in the making of the samples for batch 2. The authors also would like to thank Étienne Rimpot, Catherine Rio, Agnès Bachelier-Locq, and Pierre Beauchène, who took part in the samples preparation or characterization.

Conflict of Interest

The authors declare no conflict of interest.

Author Contributions

Baptiste Egrettau: Conceptualization (lead); Investigation (lead); Methodology (lead); Visualization (lead); Writing—original draft (lead); Writing—review & editing (equal). **Fabien Méry:** Funding acquisition (lead); Supervision (lead); Writing—original draft (equal). **Cécile Davoine:** Investigation (supporting); Methodology (supporting); Supervision (lead); Writing—original draft (supporting). **Olivier Vermeersch:** Methodology (equal); Supervision (supporting); Writing—review & editing (supporting). **Marc Thomas:** Investigation (supporting); Supervision (supporting); Writing—review & editing (supporting).

Data Availability Statement

The data that support the findings of this study are available from the corresponding author upon reasonable request.

Keywords

anisotropy, Kozeny–Carman model, porous materials, spark plasma sintering, Ti64

Received: May 7, 2024

Revised: September 19, 2024

Published online:

-
- [1] J. Cousteix, *Aérodynamique: Turbulence et Couche Limite*, Collection La Chevêche, CEPADUES, Toulouse, France **1989**.
- [2] J. D. Anderson, *Fundamentals of Aerodynamics*, 6th ed., McGraw Hill Education, New York, NY **2017**.
- [3] A. L. Braslow, *A History of Suction-Type Laminar-Flow Control with Emphasis on Flight Research*, NASA History Division, Office of Policy and Plans, NASA Headquarters, Washington, DC **1999**.
- [4] K. S. G. Krishnan, O. Bertram, O. Seibel, *Prog. Aerospace Sci.* **2017**, 93, 24.
- [5] T. Young, B. Humphreys, J. Fielding, *Aircr. Des.* **2001**, 4, 127.
- [6] G. Schrauf, H. von Geyr, *J. Aircr.* **2021**, 58, 1272.
- [7] A. Seitz, M. Horn, A. Barklage, P. Scholz, C. Badrya, R. Radespiel, *AIAA Aviation 2022 Forum*, Chicago, IL **2022**.
- [8] A. L. Braslow, D. L. Burrows, N. Tetervin, F. Visconti, *Technical Report NACA-TR-1025*, NACA, Washington, DC **1951**.
- [9] B. Egretreau, J. Methel, F. Mery, O. Vermeersch, C. Davoine, M. Forte, M. Thomas, in *56th 3AF Int. Conf. on Applied Aerodynamics*, Toulouse **2022**.
- [10] M. M. Shbeh, R. Goodall, *Adv. Eng. Mater.* **2017**, 19, 1600664.
- [11] Y. Torres, S. Lascano, J. Bris, J. Pavón, J. A. Rodriguez, *Mater. Sci. Eng., C* **2014**, 37, 148.
- [12] I.-H. Oh, N. Nomura, N. Masahashi, S. Hanada, *Scr. Mater.* **2003**, 49, 1197.
- [13] R. Yamanoglu, N. Gulsoy, E. Olevsky, H. Gulsoy, *J. Alloys Compd.* **2016**, 680, 654.
- [14] D. Annur, I. Kartika, S. Supriadi, B. Suharno, *Mater. Res. Express* **2021**, 8, 012001.
- [15] M. Shi, S. Liu, Q. Wang, X. Yang, G. Zhang, *Materials* **2018**, 11, 2510.
- [16] W. Xie, J. He, S. Zhu, T. Holgate, S. Wang, X. Tang, Q. Zhang, T. M. Tritt, *J. Mater. Res.* **2011**, 26, 1791.
- [17] L. Cao, W. Zeng, Y. Xie, J. Liang, D. Zhang, *Mater. Sci. Eng., A* **2019**, 764, 138246.
- [18] D. Jafari, W. W. Wits, B. J. Geurts, *Appl. Therm. Eng.* **2018**, 143, 403.
- [19] X. Huang, G. Franchi, F. Cai, *J. Porous Mater.* **2009**, 16, 165.
- [20] F. Dominguez Espinosa, T. Peters, J. Brisson, *Int. J. Heat Mass Transfer* **2012**, 55, 7471.
- [21] G. Molénat, M. Thomas, J. Galy, A. Couret, *Adv. Eng. Mater.* **2007**, 9, 667.
- [22] D. Dudina, B. Bokhonov, E. Olevsky, *Materials* **2019**, 12, 541.
- [23] F. Zhang, E. Otterstein, E. Burkel, *Adv. Eng. Mater.* **2010**, 12, 863.
- [24] P. C. Carman, *J. Agric. Sci.* **1939**, 29, 262.
- [25] J. Methel, M. Forte, O. Vermeersch, G. Casalis, *Exp. Fluids* **2022**, 63, 21.
- [26] J. T. Gostick, Z. A. Khan, T. G. Tranter, M. D. Kok, M. Agnaou, M. Sadeghi, R. Jervis, *J. Open Source Software* **2019**, 4, 1296.
- [27] J. Fu, H. R. Thomas, C. Li, *Earth-Sci. Rev.* **2021**, 212, 103439.
- [28] T. Tranter, M. Kok, M. Lam, J. Gostick, *SoftwareX* **2019**, 10, 100277.
- [29] M. A. B. Promentilla, T. Sugiyama, T. Hitomi, N. Takeda, *Cem. Concr. Res.* **2009**, 39, 548.
- [30] M. Kaviany, *Principles of Heat Transfer in Porous Media*, Springer Science & Business Media, New York, NY **2012**.
- [31] F. A. L. Dullien, *Porous Media: Fluid Transport and Pore Structure*, Academic Press, New York **1979**.
- [32] J. Methel, *Ph.D Thesis*, ISAE-Supaéro, Université de Toulouse **2019**.
- [33] I. H. Oh, H. T. Son, C. S. Kang, J. S. Lee, J. I. Cho, J. C. Bae, B. T. Lee, H. Y. Song, *Mater. Sci. Forum* **2007**, 539–543, 635.
- [34] R. Roncen, Z. E. A. Fellah, E. Ogam, *J. Sound Vib.* **2022**, 520, 116601.
- [35] K. V. Horoshenkov, A. Hurrell, J.-P. Groby, *J. Acoust. Soc. Am.* **2019**, 145, 2512.